

Supercontinuum generation in quasi-phasematched waveguides

C. R. Phillips,^{1,*} Carsten Langrock,¹ J. S. Pelc,¹ M. M. Fejer,¹
I. Hartl,² and Martin E. Fermann²

¹Edward L. Ginzton Laboratory, Stanford University, Stanford, California 94305-4085, USA

²IMRA America, Inc., Ann Arbor, Michigan 48105, USA

[*chris.phillips@stanford.edu](mailto:chris.phillips@stanford.edu)

Abstract: We numerically investigate supercontinuum generation in quasi-phase-matched waveguides using a single-envelope approach to capture second and third order nonlinear processes involved in the generation of octave-spanning spectra. Simulations are shown to agree with experimental results in reverse-proton-exchanged lithium-niobate waveguides. The competition between $\chi^{(2)}$ and $\chi^{(3)}$ self phase modulation effects is discussed. Chirped quasi-phasematched gratings and stimulated Raman scattering are shown to enhance spectral broadening, and the pulse dynamics involved in the broadening processes are explained.

© 2011 Optical Society of America

OCIS codes: (320.6629) Supercontinuum generation; (190.4410) Nonlinear optics, parametric processes.

References and links

1. C. Langrock, M. M. Fejer, I. Hartl, and M. E. Fermann, "Generation of octave-spanning spectra inside reverse-proton-exchanged periodically poled lithium niobate waveguides," *Opt. Lett.* **32**, 2478–2480 (2007).
2. T. Fuji, J. Rauschenberger, A. Apolonski, V. S. Yakovlev, G. Tempea, T. Udem, C. Gohle, T. W. Hänsch, W. Lehnert, M. Scherer, and F. Krausz, "Monolithic carrier-envelope phase-stabilization scheme," *Opt. Lett.* **30**, 332–334 (2005).
3. J. M. Dudley, G. Genty, and S. Coen, "Supercontinuum generation in photonic crystal fiber," *Rev. Mod. Phys.* **78**, 1135–1184 (2006).
4. J. Price, T. Monro, H. Ebendorff-Heidepriem, F. Poletti, P. Horak, V. Finazzi, J. Leong, P. Petropoulos, J. Flanagan, G. Brambilla, X. Feng, and D. Richardson, "Mid-IR supercontinuum generation from nonsilica microstructured optical fibers," *IEEE J. Sel. Top. Quantum Electron.* **13**, 738–749 (2007).
5. C. R. Phillips and M. M. Fejer, "Stability of the singly resonant optical parametric oscillator," *J. Opt. Soc. Am. B* **27**, 2687–2699 (2010).
6. C. Langrock, S. Kumar, J. McGeehan, A. Willner, and M. M. Fejer, "All-optical signal processing using $\chi^{(2)}$ nonlinearities in guided-wave devices," *J. Lightwave Technol.* **24**, 2579–2592 (2006).
7. X. Yu, L. Scaccabarozzi, J. S. Harris, P. S. Kuo, and M. M. Fejer, "Efficient continuous wave second harmonic generation pumped at 1.55 μm in quasi-phase-matched AlGaAs waveguides," *Opt. Express* **13**, 10742–10748 (2005).
8. M. Conforti, F. Baronio, and C. De Angelis, "Nonlinear envelope equation for broadband optical pulses in quadratic media," *Phys. Rev. A* **81**, 053841 (2010).
9. R. V. Roussev, "Optical-frequency mixers in periodically poled lithium niobate: materials, modeling and characterization," Ph.D. thesis, Stanford University (2006), http://nlo.stanford.edu/system/files/dissertations/rostitlav_roussev_thesis_december_2006.pdf.
10. M. Kolesik and J. V. Moloney, "Nonlinear optical pulse propagation simulation: from Maxwell's to unidirectional equations," *Phys. Rev. E* **70**, 036604 (2004).
11. G. Genty, P. Kinsler, B. Kibler, and J. M. Dudley, "Nonlinear envelope equation modelling of sub-cycle dynamics and harmonic generation in nonlinear waveguides," *Opt. Express* **15**, 5382–5387 (2007).
12. M. Conforti, F. Baronio, and C. De Angelis, "Ultrabroadband optical phenomena in quadratic nonlinear media," *IEEE Photon. J.* **2**, 600–610 (2010).

13. S. Wabnitz and V. V. Kozlov, "Harmonic and supercontinuum generation in quadratic and cubic nonlinear optical media," *J. Opt. Soc. Am. B* **27**, 1707–1711 (2010).
14. G. Imeshev, M. M. Fejer, A. Galvanauskas, and D. Harter, "Pulse shaping by difference-frequency mixing with quasi-phase-matching gratings," *J. Opt. Soc. Am. B* **18**, 534–539 (2001).
15. M. M. Fejer, G. A. Magel, D. H. Jundt, and R. L. Byer, "Quasi-phase-matched second harmonic generation: tuning and tolerances," *IEEE J. Quantum Electron.* **28**, 2631–2654 (1992).
16. X. Liu, L. Qian, and F. W. Wise, "High-energy pulse compression by use of negative phase shifts produced by the cascade $\chi^{(2)} : \chi^{(2)}$ nonlinearity," *Opt. Lett.* **24**, 1777–1779 (1999).
17. J. Moses and F. W. Wise, "Soliton compression in quadratic media: high-energy few-cycle pulses with a frequency-doubling crystal," *Opt. Lett.* **31**, 1881–1883 (2006).
18. S. Ashihara, J. Nishina, T. Shimura, and K. Kuroda, "Soliton compression of femtosecond pulses in quadratic media," *J. Opt. Soc. Am. B* **19**, 2505–2510 (2002).
19. M. Bache, O. Bang, J. Moses, and F. W. Wise, "Nonlocal explanation of stationary and nonstationary regimes in cascaded soliton pulse compression," *Opt. Lett.* **32**, 2490–2492 (2007).
20. M. Bache and F. W. Wise, "Type-I cascaded quadratic soliton compression in lithium niobate: compressing femtosecond pulses from high-power fiber lasers," *Phys. Rev. A* **81**, 053815 (2010).
21. J. Gordon, "Theory of the soliton self-frequency shift," *Opt. Lett.* **11**, 662–664 (1986).
22. M. Charbonneau-Lefort, B. Afeyan, and M. M. Fejer, "Optical parametric amplifiers using chirped quasi-phase-matching gratings I: practical design formulas," *J. Opt. Soc. Am. B* **25**, 463–480 (2008).
23. C. R. Phillips and M. M. Fejer, "Efficiency and phase of optical parametric amplification in chirped quasi-phase-matched gratings," *Opt. Lett.* **35**, 3093–3095 (2010).
24. C. Heese, C. R. Phillips, L. Gallmann, M. M. Fejer, and U. Keller, "Ultrabroadband, highly flexible amplifier for ultrashort midinfrared laser pulses based on aperiodically poled Mg:LiNbO₃," *Opt. Lett.* **35**, 2340–2342 (2010).
25. R. DeSalvo, A. Said, D. Hagan, E. Van Stryland, and M. Sheik-Bahae, "Infrared to ultraviolet measurements of two-photon absorption and n_2 in wide bandgap solids," *IEEE J. Quantum Electron.* **32**, 1324–1333 (1996).
26. I. Shoji, T. Kondo, A. Kitamoto, M. Shirane, and R. Ito, "Absolute scale of second-order nonlinear-optical coefficients," *J. Opt. Soc. Am. B* **14**, 2268–2294 (1997).
27. M. Bache, O. Bang, B. B. Zhou, J. Moses, and F. W. Wise, "Optical cherenkov radiation in ultrafast cascaded second-harmonic generation," *Phys. Rev. A* **82**, 063806 (2010).
28. C. R. Phillips, J. Jiang, C. Langrock, M. M. Fejer, and M. E. Fermann, "Self-Referenced Frequency Comb From a Tm-fiber Amplifier via PPLN Waveguide Supercontinuum Generation," in *CLEO:2011 - Laser Applications to Photonic Applications*, OSA Technical Digest (CD) (Optical Society of America, 2011), paper PDP A5.
29. A. S. Barker and R. Loudon, "Dielectric properties and optical phonons in LiNbO₃," *Phys. Rev.* **158**, 433 (1967).
30. P. J. Delfyett, R. Dorsinville, and R. R. Alfano, "Spectral and temporal measurements of the third-order nonlinear susceptibility of LiNbO₃ using picosecond Raman-induced phase-conjugate spectroscopy," *Phys. Rev. B* **40**, 1885 (1989).
31. N. Surovtsev, V. Malinovskii, A. Pugachev, and A. Shebanin, "The nature of low-frequency raman scattering in congruent melting crystals of lithium niobate," *Phys. Solid State* **45**, 534–541 (2003).
32. R. Schiek, R. Stegeman, and G. I. Stegeman, "Measurement of third-order nonlinear susceptibility tensor elements in lithium niobate," in "Frontiers in Optics," (Optical Society of America, 2005), p. JWA74.
33. G. I. Stegeman, D. J. Hagan, and L. Torner, " $\chi^{(2)}$ cascading phenomena and their applications to all-optical signal processing, mode-locking, pulse compression and solitons," *Opt. Quantum Electron.* **28**, 1691–1740 (1996).
34. C. Conti, S. Trillo, P. Di Trapani, J. Kilius, A. Bramati, S. Minardi, W. Chinaglia, and G. Valiulis, "Effective lensing effects in parametric frequency conversion," *J. Opt. Soc. Am. B* **19**, 852–859 (2002).
35. D. H. Jundt, "Temperature-dependent Sellmeier equation for the index of refraction, n_e , in congruent lithium niobate," *Opt. Lett.* **22**, 1553–1555 (1997).
36. R. Boyd, "Stimulated Raman scattering and stimulated Rayleigh-Wing scattering," in "Nonlinear Optics," R. Boyd (Academic, 2008).
37. C. Heese, C. R. Phillips, L. Gallmann, M. M. Fejer, and U. Keller, "High-power mid-infrared optical parametric chirped-pulse amplifier based on aperiodically poled Mg:LiNbO₃," presented at the Conference on Lasers and Electro-optics (2011).
38. E. D. Palik and G. Ghosh, *Handbook of Optical Constants of Solids* (Academic, 1985).

1. Introduction

The generation of coherent light in the infrared from mode-locked lasers is of considerable interest for applications including frequency comb generation, spectroscopy, and few-cycle pulse generation [1–4]. Absolute frequency calibration is usually achieved by self-referencing, for example via 1f-2f or 2f-3f interferometry [1, 2]. To perform self-referencing and to reach spectral regions not accessible through suitable or well-developed laser gain media, nonlinear-optical

methods are usually required. Optical parametric oscillators (OPOs) can be used to span the mid-IR, but are complex and additional steps must be taken for self-referencing and, in some cases, to ensure stability [5]. Much attention has also been given to $\chi^{(3)}$ -based supercontinuum generation in optical fibers [3]. Due to the high nonlinearity and engineerable dispersion available in fibers, spectra spanning multiple octaves can be achieved. This process is limited by the transparency window of the fiber; extending supercontinuum generation to non-silica fibers transparent in the mid-IR is an active area of research [4].

Compared to fibers, relatively little attention has been given to supercontinuum generation via $\chi^{(2)}$ processes in quasi-phasematched (QPM) media, even though very high nonlinearities are readily available in QPM waveguides [6], and supercontinuum generation has been demonstrated experimentally [1, 2]. In contrast to methods employing bulk QPM media, QPM waveguides enable highly nonlinear interactions when pumping with commercial mode-locked lasers (including fiber lasers) with few-nJ pulse energies. Additionally, nonlinear interactions have been demonstrated in QPM waveguides using GaAs [7], which has transparency up to 17 μm and therefore offers the possibility of generating a supercontinuum across the mid-IR. In order to reach this goal, a detailed understanding and quantitative modeling of the nonlinear dynamics involved is first required. Progress has been made recently in modeling broadband $\chi^{(2)}$ interactions [8], but a complete analysis including waveguide effects, competing nonlinearities, and the role that chirped QPM gratings can play in enhancing spectral broadening has not yet been performed. In order to reach the full potential of QPM waveguides for continuum generation, these effects must be modeled so that appropriate QPM gratings and, where necessary, dispersion-engineered waveguides can be designed.

In this paper, we develop a model to describe nonlinear interactions in QPM waveguides. In order to test and calibrate the model, we simulate the experiments of Ref. [1], which were performed in reverse proton exchanged (RPE) LiNbO₃ waveguides, and show good agreement between experiments and simulations. Our analysis reveals the importance of several effects including the $\chi^{(2)}$ and instantaneous $\chi^{(3)}$ nonlinearities, stimulated Raman scattering (SRS; χ_R), the interaction between multiple waveguide modes, and the dispersion of the waveguides and associated modal overlaps. The required modal properties of the RPE waveguides are determined from a proton concentration profile calculated with the concentration-dependent diffusion model given in Ref. [9]. In section 2 we introduce our nonlinear waveguide model. In section 3, the results of our model are compared to the 1043-nm-pumped experiments of Ref. [1]. In section 4 and appendices A and B, we show the importance of different $\chi^{(2)}$ and $\chi^{(3)}$ terms in reproducing the experimental results, and discuss how the model parameters were estimated in cases where absolute values could not be determined from available literature data. In section 5, our model is compared to the 1580-nm-pumped experiments of [1].

2. Numerical model

In this section, we introduce a model to simulate ultra-broadband nonlinear interactions between multiple waveguide modes using an analytic-signal formalism for forward-propagating waves, similar to that described in Refs. [8, 10–13], generalized to describe waveguide interactions with multiple nonlinear optical effects and multiple guided modes. The model automatically accounts for all of the conventional $\chi^{(2)}$ interactions including second harmonic generation (SHG), sum frequency generation (SFG), and difference frequency generation (DFG) including intrapulse DFG. All $\chi^{(3)}$ interactions can be accounted for as well, but we consider only self and cross phase modulation (SPM and XPM), and SRS. Our analysis is suited to weakly-guided modes such as in RPE LiNbO₃ waveguides, but could be generalized to describe tightly-confined modes.

First, the spectrum of the total electric field is expanded in terms of a sum of waveguide

modes

$$\tilde{E}(x, y, z, \omega) = \frac{1}{2} \sum_n B_n(x, y, \omega) \tilde{A}_n(z, \omega - \omega_{\text{ref}}) \exp[-i(\beta_{\text{ref}} - \omega_{\text{ref}}/v_{\text{ref}})z], \quad (1)$$

where \tilde{E} is a Fourier component of the real-valued electric field $E(x, y, z, t)$ (tilde denotes a frequency-domain field quantity) and the optical frequency $\omega > 0$. The real-valued transverse spatial mode profiles of the bound modes are given by B_n and the z-dependent envelopes by \tilde{A}_n . We assume that $\tilde{A}_n(z, \omega < 0) = 0$ (i.e. \tilde{A}_n are analytic signals). We have also defined a reference propagation constant β_{ref} , a reference group velocity v_{ref} , and a carrier frequency ω_{ref} ; appropriate choices for these reference quantities are discussed below. From Ref. [14], the nonlinear polarization can be expressed in the frequency domain as

$$\begin{aligned} \tilde{P}_{NL}(\omega)/\epsilon_0 = & \int_{-\infty}^{\infty} \chi^{(2)}(\omega, \omega', \omega - \omega') \tilde{E}(\omega') \tilde{E}(\omega - \omega') d\omega' + \\ & \int_{-\infty}^{\infty} \int_{-\infty}^{\infty} \chi^{(3)}(\omega, \omega', \omega'', \omega - \omega' - \omega'') \tilde{E}(\omega') \tilde{E}(\omega'') \tilde{E}(\omega - \omega' - \omega'') d\omega' d\omega''. \end{aligned} \quad (2)$$

To calculate the nonlinear coupling between envelopes \tilde{A}_n , suitable integrations involving \tilde{P}_{NL} are performed over the transverse spatial dimensions x and y of the waveguide. For the $\chi^{(2)}$ nonlinear term, these modal overlap integrals are given by

$$\Theta_{npq}(\omega, \omega') = \int_{-\infty}^{\infty} \tilde{\chi}^{(2)}(x, y; \omega, \omega', \omega - \omega') B_n(x, y, \omega) B_p(x, y, \omega') B_q(x, y, \omega - \omega') dx dy. \quad (3)$$

Since the magnitude of the second-order nonlinearity has a spatial dependence due to non-idealities of the waveguide fabrication process [9], we have introduced a normalized susceptibility $\tilde{\chi}^{(2)} = |\chi^{(2)}(x, y)/\chi_0^{(2)}|$, where $\chi_0^{(2)}$ is the relevant tensor element in the unperturbed material. For RPE LiNbO₃ waveguides, $|\chi^{(2)}(x, y)|$ is negligible close to the upper surface of the crystal, down to a depth h_{WG} below the surface [9]. Therefore, $\tilde{\chi}^{(2)}(x, y) = 0$ for $y < h_{\text{WG}}$ and $\tilde{\chi}^{(2)}(x, y) = 1$ for $y \geq h_{\text{WG}}$, where $y = 0$ denotes the upper surface of the crystal.

Propagation equations for $\tilde{A}_n(z)$ can be derived using Eqs. (2) and (3), but involve time-consuming integrals in the frequency domain, particularly for the $\chi^{(3)}$ terms. To derive a simple yet accurate propagation equation, note that the scale of $B_n(x, y, \omega)$ in Eq. (1) is arbitrary since any frequency-dependent scale factor applied to B_n can be absorbed into \tilde{A}_n . Hence, B_n can be chosen so as to minimize the frequency-dependence of the overlap integral for the fundamental waveguide mode, Θ_{000} , given in Eq. (3). We therefore introduce a frequency dependent normalization for the modes, according to

$$\int_{-\infty}^{\infty} |B_n(x, y, \omega)|^2 dx dy = g_n(\omega) \quad (4)$$

where the form of $g_n(\omega)$ is chosen to simplify the numerics. To satisfy Eq. (4), we define $B_n(x, y, \omega) \equiv (g_n(\omega))^{1/2} \bar{B}_n(x, y, \omega) / (\int_{-\infty}^{\infty} |\bar{B}_n(x, y, \omega)|^2 dx dy)^{1/2}$, where $\bar{B}_n(x, y, \omega)$ are numerically-determined, un-normalized mode profiles. The strength of the nonlinear interactions will generally scale inversely with the mode area, which we define as $a_n(\omega) \equiv (\int_{-\infty}^{\infty} |\bar{B}_n|^2 dx dy)^2 / (\int_{-\infty}^{\infty} |\bar{B}_n|^4 dx dy)$ for mode n at frequency ω . We choose $g_n(\omega) = a_n(\omega)^{1/3}$, since this choice renders Θ_{npq} dimensionless and Θ_{000} weakly dispersive. The analogous $\chi^{(3)}$ terms Θ_{npqr} , which have a form similar to Eq. (3), are not dimensionless. As such, a single set of functions $g_n(\omega)$ cannot simultaneously account for the dependence of $\chi^{(2)}$ and $\chi^{(3)}$ modal overlap integrals on optical frequency. Despite this limitation we find that, with the above choice

of g_n , experiments can be described quantitatively while neglecting the dispersion of both the modal overlap integrals Θ_{npq} and Θ_{npqr} . The dependence of the $\chi^{(2)}$, $\chi^{(3)}$, and χ_R susceptibilities on optical frequency is neglected, but the dependence of χ_R on the Raman frequency shift, and hence the Raman response function, is retained.

Next, to determine a first-order propagation equation we neglect backwards-propagating waves [10, 11], and approximate the nonlinear coupling coefficients $\Theta_{npq}(\omega, \omega')$ and $\Theta_{npqr}(\omega, \omega', \omega'')$ as constants θ_{npq} and θ_{npqr} , respectively. The smoothly-chirped QPM grating is expanded in a Fourier series for the various QPM orders with Fourier coefficients varying slowly with z . We make use of the analytic signal formalism for the mode envelopes [8]. With these assumptions, we obtain the following set of propagation equations

$$\begin{aligned} \frac{\partial \tilde{A}_n}{\partial z} + i \left[\beta_n - \beta_{\text{ref}} - \frac{\omega - \omega_{\text{ref}}}{v_{\text{ref}}} - i \frac{\alpha_n}{2} \right] \tilde{A}_n = \\ - i \frac{\omega^2 u}{g_n \beta_n c^2} \left\{ \sum_{p,q} \sum_m d_m \theta_{npq} \mathcal{F} \left[\frac{A_p A_q}{2} e^{i\phi_m} + A_p^* A_q e^{-i\phi_m} \right] + \right. \\ \left. \sum_{p,q,r} \frac{3\theta_{npqr} \chi_E}{8} \mathcal{F} [A_p A_q^* A_r] + \sum_{p,q,r} \frac{3\theta_{npqr} \chi_{R,pk}}{8} \mathcal{F} [\mathcal{F}^{-1} [\mathcal{F} [A_p A_q^*] H_R] A_r] \right\}, \quad (5) \end{aligned}$$

where $\beta_n(\omega)$ is the modal propagation constant of mode n , and α_n is the loss coefficient of mode n , which we assume to be non-dispersive except near the 2.85 μm OH absorption feature of RPE LiNbO₃. \mathcal{F} denotes the Fourier transform, $\mathcal{F}[f(t)](\Omega) = \int f(t) \exp(-i\Omega t) dt$. The envelope phase is given by $\phi_m(z, t) = \omega_{\text{ref}} t - (\beta_{\text{ref}} - \omega_{\text{ref}}/v_{\text{ref}})z - m\phi_G(z)$, where the grating phase $\phi_G = \int_0^z K_g(z') dz'$ for local QPM grating k-vector $K_g(z)$. The QPM Fourier coefficients are given by $d_m(z) = 2d \sin(m\pi D(z))/(m\pi)$ [15], where D is the QPM duty cycle and m is the QPM order. In Eq. (5), the summation is performed over all the relevant positive and negative QPM orders, with phases $\exp(i\phi_m)$ for SFG terms (which have form $A_p A_q$), and $\exp(-i\phi_m)$ for DFG terms (form $A_p^* A_q$). In this way, each QPM order is associated with both a corresponding conjugate SFG and DFG process; this association is required for energy conservation.

For a particular input center frequency ω_c , we usually choose $\omega_{\text{ref}} \approx 2\omega_c$ and $\beta_{\text{ref}} \approx \beta_0(2\omega_c)$ (since significant spectral components up to around $3\omega_c$ or higher can be generated), and $v_{\text{ref}}^{-1} = (\partial\beta_0/\partial\omega)|_{\omega=\omega_c}$ (since only energy which remains overlapped temporally with the input pulse contributes significantly to the nonlinear dynamics). A useful property of Eq. (5) is that the nonlinear polarization can be calculated via time-domain products of mode envelopes $A_n(z, t)$. This property arises from neglecting (or simplifying, in the case of SRS) the frequency-dependence of the modal overlap integrals and nonlinear susceptibilities.

Third-order nonlinear effects are described by the final two terms in Eq. (5). In writing Eq. (5), we assume that the third-order nonlinear susceptibility can be approximated by $\chi^{(3)}(\omega; \omega - \Omega, \omega', \Omega - \omega') = \chi_E + \chi_R(\Omega)$, where χ_E is the instantaneous (frequency-independent) electronic susceptibility, and $\chi_R(\Omega)$ is the Raman susceptibility (which depends only on the Raman frequency shift Ω). We define $\chi_R(\Omega) \equiv \chi_{R,pk} H_R(\Omega)$, where $\chi_{R,pk}$ is the peak Raman susceptibility, and $H_R(\Omega)$ is the Raman transfer function; $H_R(\Omega)$ is the Fourier transform of the Raman (temporal) response function $h(t)$. The peak Raman frequency Ω_{pk} is defined as the frequency shift for which $|\Im[\chi_R]|$ is largest; H_R is normalized so that $\Im[H_R(\pm\Omega_{pk})] = \mp 1$, and the peak Raman susceptibility is defined as $\chi_{R,pk} \equiv |\Im[\chi_R(\Omega_{pk})]|$. The complex Raman transfer function is discussed in Appendix A. The values we use for the nonlinear susceptibilities are discussed in Appendix A and in section 4.

Most of the $\chi^{(2)}$ interactions modeled by Eq. (5) are highly phase mismatched. In particular, for a given process (SHG, SFG or DFG involving a particular combination of waveguide modes) usually at most one QPM order, denoted m_0 , is close to phasematching. To model a dif-

ferent QPM order m , the grid size required increases approximately in proportion to $|m - m_0|$, while the contribution to the pulse dynamics is (approximately) proportional to $1/|m - m_0|^3$. In appendix B, we discuss these terms in more detail and calculate their contribution to the total SPM of the input pulse. In some cases, instead of including higher order terms explicitly in the simulations, their leading-order contributions to the pulse dynamics can be calculated analytically via the cascading approximation, which yields an effective instantaneous $\chi^{(3)}$ coefficient for each term. These coefficients can then be added to the true instantaneous $\chi^{(3)}$ coefficient χ_E in Eq. (5), yielding an adjusted and possibly z -dependent effective value of $\chi_E(z)$.

3. Comparison to 1043-nm-pumped experiments

In this section, we test the nonlinear waveguide model given by Eq. (5) by comparing it to the 1043-nm-pumped experiments of Ref. [1]. In those experiments, broadband spectra were achieved when a particular chirped QPM grating profile was used, but not when a simple unchirped QPM grating was used. The pump pulses had a duration of 150 fs (FWHM) and an energy of approximately 3.45 nJ inside the waveguide. The QPM grating had a length of 29 mm and the grating period was varied from 7 μm to 11 μm over this length by a linear chirp (i.e. $dK_g/dz = \text{constant}$). Based on waveguide fabrication parameters and the concentration-dependent diffusion model given in Ref. [9], we estimate the area of the TM_{00} mode at 1043 nm and 521.5 nm as 16.30 μm^2 and 6.37 μm^2 , respectively. For the modal overlap integrals, $\theta_{000} \approx 0.817$, and $\theta_{0000} \approx 0.3925 \mu\text{m}^{-2/3}$ (evaluated for self phase modulation at 1043 nm). For the TM_{10} mode (mode “4”), which we also include in the model explicitly, $\theta_{400} \approx 0.162$ and the mode area at 521.5 nm is 9.80 μm^2 . We apply the waveguide cascading approximation described in appendix B to remove all but the first-order QPM interactions in Eq. (5). We assume a sech^2 input pulse profile with flat spectral phase.

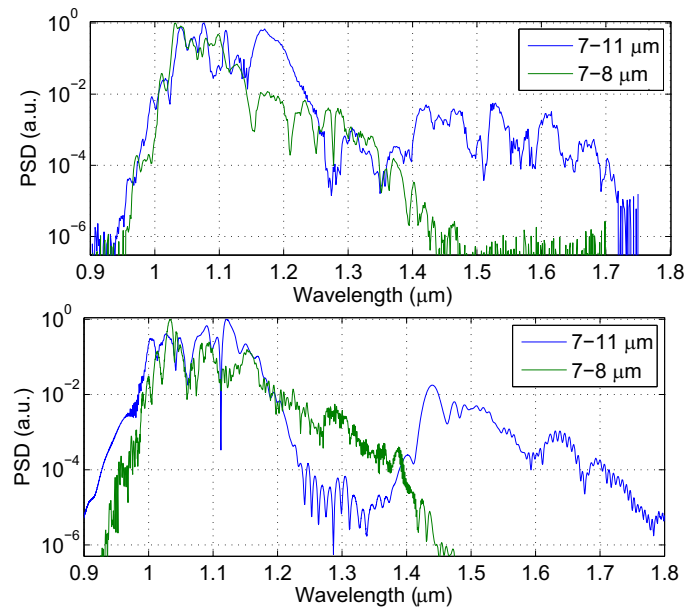


Fig. 1. Output spectrum for the 1043-nm-case of Ref. [1], labeled with the range of periods in the linearly chirped QPM grating. The pulse energy is 3.45 nJ in all cases. (a) Experimentally measured, (b) numerically simulated using Eqs. (5). A QPM grating with a weak linear chirp from 7-8 μm is included for comparison, showing reduced spectral broadening.

In Figs. 1(a) and 1(b) we show experimental and simulated output spectra corresponding to Fig. 4 of Ref. [1], respectively. The simulations are in quite good agreement with the experiments. For the 7-11 μm QPM period case, the simulation captures the main features seen experimentally, namely the high power spectral density (PSD) between 1 μm and 1.2 μm , and the “pedestal” generation between 1.4 and 1.75 μm ; the reduction in PSD between 1.2 and 1.4 μm in the experiment is also reproduced (although there is a larger reduction in the simulation). For the 7-8 μm QPM period case, the simulated spectrum falls off at approximately the same rate as in the experiment, reaching 10^{-6} of its peak at 1.45 μm . The simulated spectra were averaged over five simulations with semiclassical quantum noise seeding on the input pulse.

To understand how the spectral features in Fig. 1(b) arise, we first show in Fig. 2 the propagation of the pulse in the time domain for the case with 7-11 μm QPM period. Figure 2 represents a single simulation with no averaging. At the start of the QPM grating, the effective low-frequency $\chi^{(3)}$, $\chi_{\text{total}}^{(3)}$ [defined in Eq. (16)], is negative. This negative effective $\chi^{(3)}$ arises from cascaded $\chi^{(2)}$ interactions, and is discussed in detail in appendix B and section 4. Previous work has shown that cascaded quadratic nonlinearities by themselves can be used to support bright solitons and pulse compression, concepts closely related to supercontinuum generation [16–20]. However, near the start of the QPM grating, there is only a relatively small amount of pulse compression evident in Fig. 2(a), and similarly only a small amount of nonlinear phase is evident in Fig. 2(b), much less than would be predicted from calculations based on $\chi^{(2)}$ effects alone. This behavior occurs due to the competition between cascaded $\chi^{(2)}$ and $\chi^{(3)}$ SPM effects, which have opposite sign for this case. As a result, $\chi_{\text{total}}^{(3)}$ is initially small, and actually changes sign as the pulse propagates due to the z -dependence of the contribution from the chirped QPM grating.

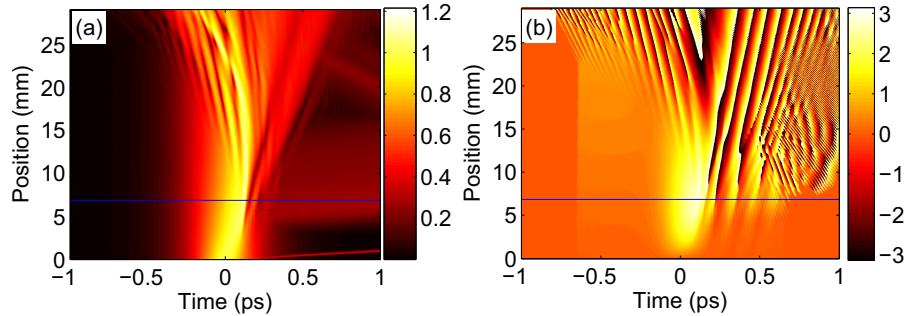


Fig. 2. Pulse evolution in the time-domain for the simulation shown in Fig. 1(b), with QPM period varied from 7-11. (a) The pulse amplitude; the color bar represents $|A_0(z, t)|$. (b) The phase of the first harmonic part of the pulse (colorbar in radians).

This change of sign of the effective $\chi^{(3)}$ can be seen in Fig. 2(b), which shows the phase of the pulse after numerically filtering out the second harmonic spectral components. An intensity-dependent phase is accumulated near the start of the QPM grating, but after approximately 7 mm, the rate of phase accumulation changes sign, suggesting that $\chi_{\text{total}}^{(3)}(z) \approx 0$ at that point. For comparison, we estimate $\chi_{\text{total}}^{(3)}(z)$ analytically with Eq. (16), evaluated for the local grating k -vector $K_g(z)$ and the local frequency of the pulse $\omega_{FH}(z)$. This latter quantity is defined by $\omega_{FH}(z) = [\int \omega |\tilde{A}_0(z, \omega)|^2 d\omega] / [\int |\tilde{A}_0(z, \omega)|^2 d\omega]$, where integration is performed only over the first harmonic (FH) region of the pulse. Equation (16) is then evaluated using $\omega_{FH}(z)$ for the frequency and $K_g(z)$ for the local grating k -vector. The solid blue lines in Fig. 2 show to

the position at which $\chi_{\text{total}}^{(3)} = 0$ according to this calculation; this position is close to where the simulated rate of phase accumulation changes sign. Thus, the initial behavior of the pulse in Fig. 2 is described quite well by this simplified picture.

Next, to understand the origin of the spectral components between 1.4 and 1.75 μm , we show in Fig. 3(a) the propagation of the pulse in the frequency domain (plotted on a log scale). The generation of spectral components $> 1.4 \mu\text{m}$ can be seen to occur around 15 mm from the start of the QPM grating. To help explain this and other processes, we show in Fig. 3(b) a simulated cross-FROG spectrogram at the output of the QPM grating, using a 150-fs Gaussian gate pulse. Due to a Raman self frequency shift (SFS) effect [21], the FH pulse shifts to lower frequencies and leaves behind a “trail” consisting of spectral components between 275 and 325 THz; simultaneously, a second harmonic (SH) wave is generated around a frequency determined by the spatial dependence of the QPM period, and also by the spatial dependence of the frequency, velocity, and propagation coefficient of the FH pulse. The generation of such waves is expected when there is a significant group index mismatch in addition to a large phase mismatch [19]. The group index difference between 521.5 and 1043 nm is ≈ 0.287 in this case, and the group velocity dispersion (GVD) is positive (and comparable to that of bulk LiNbO_3); the phase mismatch is discussed in section 4. In Fig. 3 this SH wave is shown over a limited temporal range (with delay-dependent frequencies of around 460 THz), but it extends over approximately 24 ps (with frequency increasing with delay), corresponding to the relative delay accumulated between the SH and FH frequencies over the length of the waveguide.

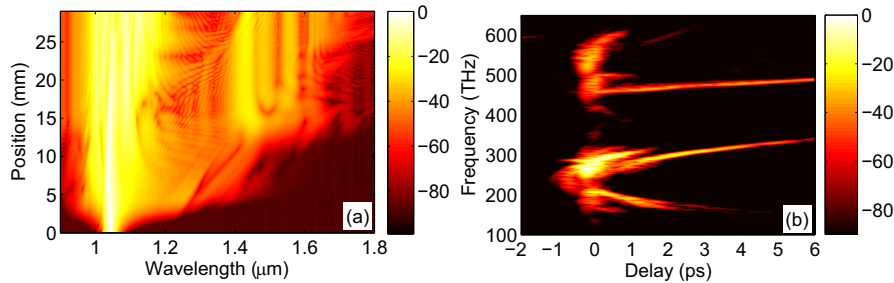


Fig. 3. (a) Spectrum versus position in the QPM grating, showing generation of spectral components $> 1.4 \mu\text{m}$ from noise. (b) Simulated cross-FROG spectrogram (150 fs gate), plotted on a dB scale. The reference velocity v_{ref} used in the simulation was the group velocity of the TM_{00} mode at 990 nm.

Due to the presence of the self frequency shifted FH pulse, its Raman trail, and the generated SH pulse, spectral components between 1.3 and 1.75 μm can be generated by at least two processes. One of these processes is optical parametric amplification (OPA) of quantum noise: spectral components between 1.4 and 1.75 μm are generated via OPA between the SH pulse (which acts as the “pump”) and quantum noise components around the input frequency. The generation of these spectral components from the (semiclassical) noise floor is evident in Fig. 3(a); when quantum noise is turned off in the simulation, these spectral components become much weaker (see Fig. 5). Because of the high SH intensities involved, the OPA process can have high gain, provided that phasematching is satisfied. The gain for this process is quite subtle, however, since the frequency and intensity of the generated SH wave depends on position z via the QPM chirp and Raman SFS of the FH pulse, and hence there is a spatially-dependent “pump” frequency and intensity; additionally, there is a spatially-dependent QPM period, and rapid temporal walk-off between pump, signal and idler spectral components. Thus, this situation differs somewhat from the chirped QPM OPA interactions studied

elsewhere [22–24], where narrow-bandwidth pumps were assumed. Nonetheless, the general model of Eq. (5) captures this effect. In the spectrogram, the amplified noise can be seen in the crescent-like pattern around the FH which extends out to approximately (6 ps, 330 THz) (for the “signal” components) and (2 ps, 170 THz) (for the “idler” components). In addition to this noise-seeded OPA process, there is a coherent process by which spectral components $> 1.3 \mu\text{m}$ are generated. This process involves the generated SH pulse mixing with the FH pulse and its Raman trail according to phasematched DFG, and can be seen in the weaker “outer” crescent-like pattern which extends to approximately (0.8 ps, 150 THz) in Fig. 3(b).

4. Model calibrations for 1043-nm-pumped experiments

In this section, we discuss which effects modeled by Eq. (5) were important in the above simulations, the sensitivity of the simulations to those effects, and how we estimate the values of the $\chi^{(3)}$ nonlinear coefficients.

In Fig. 2, we showed that the cascaded $\chi^{(2)}$ and $\chi^{(3)}$ SPM effects were of opposite sign and comparable magnitude. Here, we will quantify these terms, and hence the initial dynamics, by analyzing the $\chi^{(3)}$ and cascaded $\chi^{(2)}$ contributions to SPM near the input of the QPM grating. The effective low-frequency-shift third-order nonlinear susceptibility, $\chi_{\text{total}}^{(3)}$, is given by Eq. (16). This susceptibility determines the initial rate of SPM for narrow-bandwidth pulses. There are contributions to $\chi_{\text{total}}^{(3)}$ from χ_E , SRS, and from each waveguide mode at each order of the QPM grating via cascaded $\chi^{(2)}$ interactions. These cascaded $\chi^{(2)}$ contributions are labeled $\chi_{\text{cascade}}^{m,q}$ for QPM order m , SH waveguide mode index q and FH waveguide mode index 0, and are described in appendix B in terms of the phase mismatches $\Delta k_{m,q00}$ [defined in Eq. (14)]. The necessary parameters for calculating $\chi_{\text{cascade}}^{m,q}$ for these experiments are given in Table 2. There are also small but non-negligible nonlinear phase shifts due to cross phase modulation and cross Raman scattering from the SH acting on the FH pulse; these effects are captured by the simulations, but we neglect them for this simplified analysis.

At the input of the QPM grating (local QPM period $7 \mu\text{m}$), and with $d_{33} = 25.2 \text{ pm}^2/\text{V}^2$, $\sum \chi_{\text{cascade}}^{m,q} = 9140 \text{ pm}^2/\text{V}^2$. The largest-magnitude term is $\chi_{\text{cascade}}^{1,0} = -7915 \text{ pm}^2/\text{V}^2$, which corresponds to first-order QPM involving the lowest-order waveguide mode at the SH frequency. In appendix A, we find that for congruent LiNbO₃, $\chi_E + H_R(0) = 6365 \text{ pm}^2/\text{V}^2$. Based on this $\chi^{(3)}$ contribution, the effective low-frequency $\chi^{(3)}$ would be very small if only the lowest-order waveguide mode, first-order QPM interaction ($\chi_{\text{cascade}}^{1,0}$) was included in Eq. (5). With all the $\chi^{(2)}$ terms included, $\chi_{\text{total}}^{(3)} \approx -2775 \text{ pm}^2/\text{V}^2$ is negative, but has much lower magnitude than predictions based on the $\chi^{(2)}$ terms alone. For the remaining cascading terms, $\chi_{\text{cascade}}^{-1,1} = -830 \text{ pm}^2/\text{V}^2$ (corresponding to a negative order of the QPM grating); the next largest term is $\chi_{\text{cascade}}^{1,4} = -413 \text{ pm}^2/\text{V}^2$.

As the pulse propagates through the waveguide, the Raman SFS effect causes $\Delta k_{0,000}$ (the phase mismatch for SHG involving the lowest-order waveguide modes and with QPM order 0) to decrease, and hence decreases $\Delta k_{1,000}$ since $\Delta k_{0,000} > K_g$; however, the QPM chirp increases $\Delta k_{1,000}$ with z since $K_g(z)$ is decreasing. The net result of these two effects for this particular case is that $\chi_{\text{cascade}}^{(3)}$ actually changes sign during propagation, as shown in Fig. 2(b). Since the cancellation between the cascaded $\chi^{(2)}$ and $\chi^{(3)}$ terms hindered conventional spectral broadening via SPM, the dominant mechanism for generating spectral components $> 1.4 \mu\text{m}$ was optical parametric amplification of quantum noise. This mechanism is consistent with the results of Ref. [1], where observation of the carrier-envelope-offset frequency f_{CEO} was reported when using a 1580-nm pump, but not for the 1043-nm-pumping case. For many applications, the coherence of the supercontinuum is important; if the cancellation of SPM effects was re-

duced, the intensity of the SH could be reduced and the rate of FH SPM increased, thereby allowing for coherent supercontinuum generation.

The above analysis of SPM effects depends on the low-frequency $\chi^{(3)}$ terms, $\chi_E + H_R(0)\chi_{R,pk}$, which can be determined quite accurately. However, both $\chi^{(3)}$ parameters need to be known or estimated for the simulations; in appendix A, we show that it is difficult to use available literature data to absolutely calibrate both χ_E and $\chi_{R,pk}$ simultaneously. To show the importance of these terms beyond the $\chi^{(2)} - \chi^{(3)}$ competition calculated above, we first show that SRS must be included in the model in order to reproduce the experimental results. The importance of SRS is shown in Fig. 4, where we plot the output spectrum for several values of χ_E while setting $\chi_{R,pk} = 0$. For the case with $\chi_{R,pk} = 0$ and $\chi_E = 0$, there is a long-wavelength pedestal which extends to $> 2 \mu\text{m}$; this pedestal extends further than the spectra shown in Figs. 1(a) and 1(b). However, based on the results of appendix A, $\chi_E + H_R(0)\chi_{R,pk} \approx 6365 \text{ pm}^2/\text{V}^2$. When χ_E is increased towards this value (while still maintaining the false assumption that $\chi_{R,pk} = 0$), the spectral broadening is reduced significantly. For the $\chi_E > 3000 \text{ pm}^2/\text{V}^2$ cases in Fig. 4, the bandwidth is much narrower than in the experiments. Furthermore, for each case, there is no spectral “flattening” between 1 and $1.2 \mu\text{m}$, and no dip between 1.2 and $1.4 \mu\text{m}$; both of these spectral features can be seen in Figs. 1(a) and 1(b).

The results of Fig. 4 show that simulations with SRS neglected differ significantly from the experimental results; the results of section 3 show that when all the terms in Eq. (5) are included, our model is sufficient to reproduce the spectral features observed experimentally, without any adjustments to known model parameters. We can therefore conclude that SRS plays an important role in the dynamics and must be included in the model. Note, in particular, that including SRS leads to the spectral “flattening” shown in Figs. 1(a) and 1(b). The frequency range over which the pulse spectrum is flattened is comparable to the Raman peak with largest frequency shift ($\approx 19 \text{ THz}$) (see Fig. 7). Since this flattening also only occurs when SRS is included in the model, we can identify this effect as a Raman SFS.

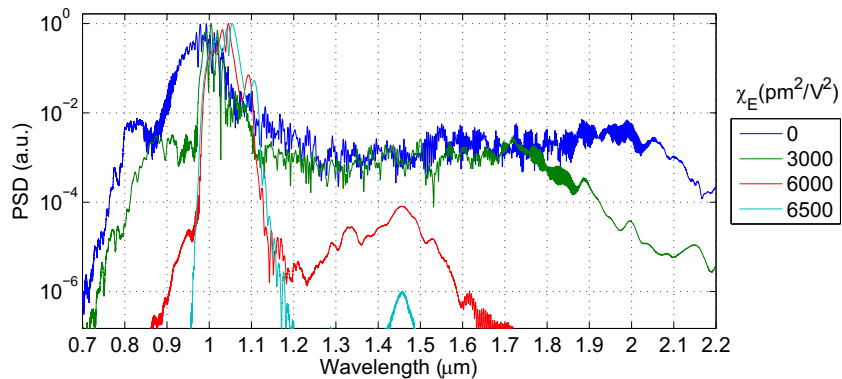


Fig. 4. Spectrum for several values of χ_E , with $\chi_{R,pk} = 0$. The values for χ_E are given in the legend in units of pm^2/V^2 ; the other model parameters are the same as those used in Fig. 1(b).

Next, we consider the values of χ_E and $\chi_{R,pk}$. To estimate these parameters, we performed simulations of the experiments discussed in section (3) for several values $\chi_{R,pk}$ at fixed $(\chi_E + H_R(0)\chi_{R,pk})$, and compared the resulting simulated spectra to the experimentally observed spectrum in Fig. 1(a). In order to agree reasonably well, the spectrum should exhibit the spectral flattening between 1 and $1.2 \mu\text{m}$ (SFS), and have a supercontinuum “pedestal” between 1.4 and $1.75 \mu\text{m}$ with a PSD around 10^{-3} less than the peak. To illustrate this numerical

procedure, we show in Fig. 5 example spectra for several representative values of $\chi_{R,pk}$ at fixed $\chi_E + H_R(0)\chi_{R,pk}$; the spectra are averaged over five simulations for each value of $\chi_{R,pk}$. For the dashed black line in Fig. 5, quantum noise was neglected. This case is plotted in order to indicate the importance of noise amplification in these simulations, as discussed in section 3. In comparing the spectrum as a function of $\chi_{R,pk}$ to the experimental results in Fig. 1(a), we find that for values of $\chi_{R,pk} < 5000 \text{ pm}^2/\text{V}^2$ the long-wavelength pedestal is weaker and extends to shorter wavelengths, and the spectral broadening between 1 and $1.2 \mu\text{m}$ is reduced; for $\chi_{R,pk} > 6000 \text{ pm}^2/\text{V}^2$, the opposite trends hold. Therefore, based on simulations similar to those in Fig. 5, we estimate $\chi_E = 5.46 \times 10^3 \text{ pm}^2/\text{V}^2$ and $\chi_{R,pk} = 5.30 \times 10^3 \text{ pm}^2/\text{V}^2$.

In relation to Fig. 3(b), increasing $\chi_{R,pk}$ increases the intensity of the generated SH wave (the part of the SH which extends to $> 6 \text{ ps}$ in the spectrogram), and hence the OPA gain (since this SH wave acts as the pump for the OPA process), which in turn leads to a stronger $> 1.4\text{-}\mu\text{m}$ pedestal generation, which corresponds to the trends shown in Fig. 5. Since the Raman SFS process broadens the FH pulse bandwidth (primarily over the $1\text{-}1.2 \mu\text{m}$ range), it might be interpreted as enhancing the non-local cascading response [19]; analogously, if the FH pulse is broadened by the SFS process such that it contains spectral components closer to phasematching, increased up-conversion can be expected, and hence a more intense SH.

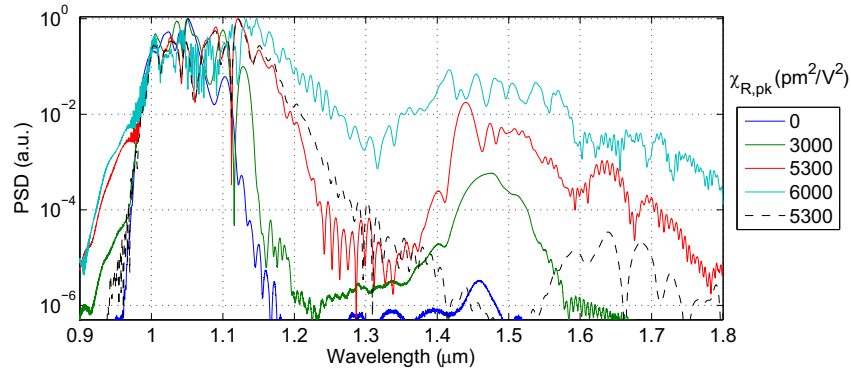


Fig. 5. Spectrum for several values of $\chi_{R,pk}$ (in pm^2/V^2) with fixed $\chi_E + H_R(0)\chi_{R,pk} = 6.365 \times 10^3 \text{ pm}^2/\text{V}^2$; the other model parameters are the same as those used in Fig. 1(b). For the dashed black line, quantum noise was neglected.

In section 5, we show that $\chi^{(3)}$ effects are also important for the 1580-nm-pumped experiments of Ref. [1], and use the same nonlinear coefficients there as those discussed in this section, with χ_E scaled by a factor close to theoretical predictions [25], to accurately model those experiments as well; this agreement suggests that the $\chi^{(3)}$ parameters estimated here are realistic. However, due to the $\chi^{(2)} - \chi^{(3)}$ competition, our simulations are sensitive to relatively small deviations in the model parameters and input conditions from our assumptions. In particular, such variations could arise from differences in $\chi^{(2)}$ and $\chi^{(3)}$ between protonated and congruent LiNbO_3 , the frequency-dependence of the $\chi^{(2)}$ and $\chi^{(3)}$ susceptibilities, and the input pulse chirp. Direct measurements of the $\chi^{(3)}$ susceptibilities in future work would be of great value for modeling supercontinuum generation in QPM media.

5. Comparison to 1580-nm-pumped experiments

To test the nonlinear waveguide model further, in this section we compare it to the 1580-nm-pumped experiments of [1]. Those experiments used pulses with a duration of 50 fs (FWHM) and energy of 1.2 nJ inside the waveguide. The QPM grating was 17.4-mm long with a grating

period of $27.5 \mu\text{m}$ and losses of approximately 0.1 dB/cm . The area of the TM_{00} mode at 1580 nm and 790 nm is estimated as $28.48 \mu\text{m}^2$ and $11.35 \mu\text{m}^2$, respectively. The modal overlap integral $\theta_{000} \approx 0.793$, and $\theta_{0000} \approx 0.3266 \mu\text{m}^{-2/3}$ (evaluated for self phase modulation at 1580 nm). For the TM_{02} mode (“mode 2”), $\theta_{002} \approx 0.043$; for the TM_{10} mode (“mode 4”), $\theta_{004} \approx 0.220$; the areas at 790 nm for these modes are $17.55 \mu\text{m}^2$ and $19.09 \mu\text{m}^2$, respectively. The remaining terms θ_{npq} are relatively small and mainly give rise to additional peaks in the pulse spectrum at short wavelengths without altering the spectral broadening very significantly.

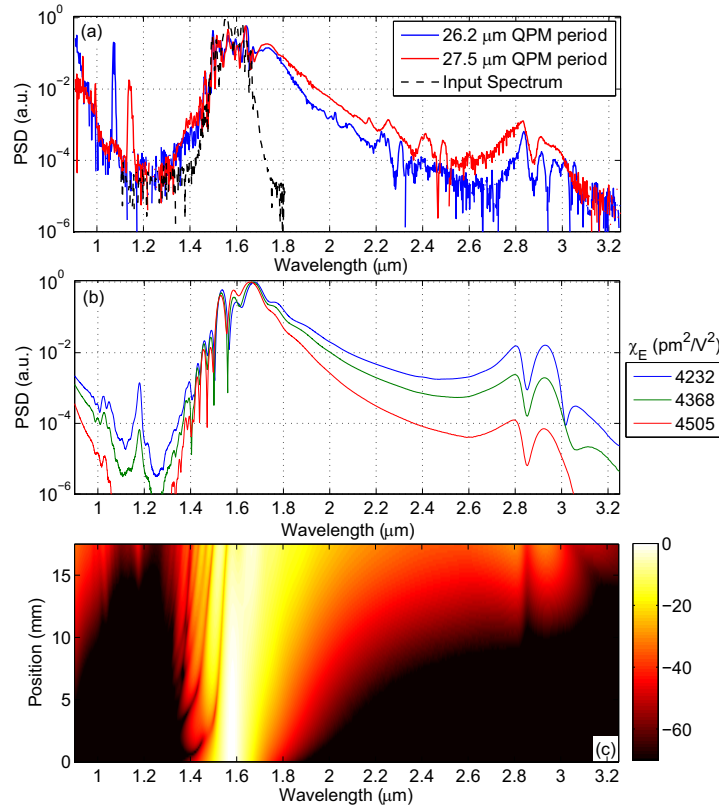


Fig. 6. (a) Experimental data with 1580-nm -pumping from Ref. [1] (b) Simulated output spectrum corresponding to (a) for the TM_{00} , TM_{10} , and TM_{02} modes. Three slightly different values of χ_E have been assumed; these values are explained in the text. (c) Evolution of the spectrum of the TM_{00} mode through the waveguide (dB scale).

In Fig. 6(a) we show the experimental results for continuum generation from Fig. 3 of Ref. [1]; in Fig. 6(b) we show simulations of these experiments using Eqs. (5) for three slightly different values of χ_E , with the TM_{00} and TM_{10} modes and the QPM orders $+1$, $+3$, and $+5$ [index m in Eq. (5)] included in the model, and assuming a 1.2-nJ input pulse. The remaining modes and QPM orders are accounted for via the cascading approximation given by Eq. (16). The simulations capture the spectral broadening observed experimentally, particularly the $\chi_E = 4368 \text{ pm}^2/\text{V}^2$ case; the evolution of the spectrum of the pulse for that case is shown in Fig. 6(c). Semiclassical quantum noise on the input pulses was included, as in sections 3 and 4, but did not change the output spectra.

The initial dynamics (near the start of the QPM grating) can be described quite accurately via the cascading approximation, discussed in appendix B and applied in section 4. Table 3 gives

the relevant parameters for evaluating the cascaded $\chi^{(2)}$ terms, $\chi_{\text{cascade}}^{m,q}$ (QPM order m and SH mode q) for SHG of the 1580-nm input pulse. With $d_{33} = 19.5 \text{ pm/V}$ [26], $\Sigma \chi_{\text{cascade}}^{m,q} = -5900 \text{ pm}^2/\text{V}^2$. The three largest-magnitude cascaded- $\chi^{(2)}$ terms are $\chi_{\text{cascade}}^{1,0} = -4416 \text{ pm}^2/\text{V}^2$, $\chi_{\text{cascade}}^{-1,0} = -1058 \text{ pm}^2/\text{V}^2$, and $\chi_{\text{cascade}}^{1,4} = -473 \text{ pm}^2/\text{V}^2$. With the value of $\chi_E + H_R(0)\chi_{R,pk}$ determined in appendix A combined with these cascade contributions, the total effective $\chi^{(3)}$ is $\chi_{\text{total}}^{(3)} = 465 \text{ pm}^2/\text{V}^2$, of the wrong sign for soliton formation. However, based on a theoretical two-band model, it is predicted that χ_E should decrease with wavelength [25]. When such a scaling of χ_E with frequency is included such that $\chi_E(1580 \text{ nm}) \approx 4368 \text{ pm}^2/\text{V}^2$, $\chi_{\text{total}}^{(3)} = -626 \text{ pm}^2/\text{V}^2$, which then supports soliton formation given the positive GVD of LiNbO₃ (and RPE waveguides) at 1580 nm. With this value of χ_E , the simulations are in good agreement with the experimental results. This scaling corresponds to $\chi_E(1580 \text{ nm})/\chi_E(1043 \text{ nm}) = 0.8$, which is very close to the predictions from the (oversimplified) two-band model. Note, however, that due to the almost complete cancellation of $\chi^{(3)}$ and $\chi^{(2)}$ contributions to the total SPM, χ_{total} and hence the output spectrum is sensitive to errors in χ_E and d_{33} of as little as 2%. This sensitivity is illustrated in Fig. 6(b), where the three χ_E cases shown correspond to values for $\chi_E(1580\text{nm})/\chi_E(1043\text{nm})$ of 0.775, 0.8, and 0.825. For more accurate modeling, it would be necessary to know the model parameters precisely, or to operate in a regime where the $\chi^{(2)} - \chi^{(3)}$ cancellation is not so complete.

With the above scaled values of χ_E , 1580 nm pulse broadens in spectrum and compresses in time due to the negative $\chi_{\text{total}}^{(3)}$, positive dispersion, and high intensity. This process is determined by the combined effects of SPM, group velocity dispersion (GVD), group velocity mismatch (GVM), and SRS. Once enough spectral broadening has occurred, various short-wavelength peaks in the spectrum are generated via phasematched processes involving different waveguide modes and QPM orders.

In the experiments, a peak in the PSD occurred around 2.85 μm and was of comparable magnitude and wavelength for different QPM periods, as shown in Fig. 6(a). Similarly, we found that the wavelength of the long-wavelength peak in the simulations is only weakly dependent on QPM period (i.e. a peak occurs at the same wavelength for a relatively wide range of QPM periods, as long as there is sufficient spectral broadening). For conventional DFG of frequency $\omega_{DFG} = \omega_1 - \omega_2$, one normally would anticipate $\Delta k = \beta(\omega_1) - \beta(\omega_2) - \beta(\omega_{DFG}) - K_g$, and thus a wavelength for the phasematched peak that would depend strongly on the QPM period, in contrast to the observed behavior. However, for a DFG process involving a phase mismatched second harmonic (SH) component as one of the participating waves, the phasematching condition differs from the conventional one.

Consider a FH pulse with center frequency ω_{FH} , effective soliton propagation constant $\beta_{\text{eff}}^{(FH)}(\omega) \approx \beta_0(\omega_{FH}) + (\omega - \omega_{FH})/v_{FH}$, and group velocity $v_{FH} \approx (\partial\beta_0(\omega_{FH})/\partial\omega)^{-1}$. The effective propagation coefficient for the phase mismatched SH pulse at frequencies ω in the vicinity of $2\omega_{FH}$ is given approximately by $\beta_{\text{eff}}^{(SH)}(\omega) \approx 2\beta_0(\omega_{FH}) + K_g + (\omega - 2\omega_{FH})/v_{FH}$. This form arises for a SH pulse $\pi/2$ radians out of phase with its driving polarization, aligned temporally with the FH pulse at group velocity v_{FH} . For the DFG process involving such a SH spectral component with frequency ω_2 , a FH spectral component with frequency ω_1 , and a generated wave at frequency $\omega_{DFG} = \omega_2 - \omega_1$, the effective Δk is given by

$$\Delta k_{\text{eff}}(\omega_{DFG}, \omega_2) = \beta_{\text{eff}}^{(SH)}(\omega_{DFG} + \omega_1) - \beta_{\text{eff}}^{(FH)}(\omega_1) - \beta_0(\omega_{DFG}) - K_g. \quad (6)$$

With the approximate forms of the propagation constants $\beta_{\text{eff}}^{(j)}$ described above,

$$\Delta k_{\text{eff}}(\omega_{DFG}) \approx \beta_0(\omega_{FH}) + (\omega_{DFG} - \omega_{FH})/v_{FH} - \beta_0(\omega_{DFG}), \quad (7)$$

independent of K_g , in contrast to the conventional phasematching relation. This type of phase-matching relation was discussed in [27]. There is a dip in the spectra at $2.85 \mu\text{m}$: this dip occurs due to OH absorption, which we included in the model as a complex Lorentzian perturbation to the effective index, with a corresponding peak absorption of 3 mm^{-1} .

The wavelength of the above cascaded DFG peak depends sensitively on the waveguide dispersion. With the dispersion relation for the lowest-order mode calculated from our concentration-dependent proton-diffusion model and the dispersion relation for protonated lithium niobate given in Ref. [9], the wavelength of the cascaded DFG peak is $> 3 \mu\text{m}$, longer than observed experimentally. However, this waveguide model is calibrated primarily for wavelengths $< 2 \mu\text{m}$. Furthermore, small changes in fabrication parameters could also lead to shifts in the effective phase mismatch given by Eq. (7). Therefore, some discrepancy with experiments can be expected for processes involving longer wavelengths. The wavelength of the cascaded DFG peak also depends on the pulse frequency, which changes due to the Raman SFS. This SFS depends on the value of $\chi_{R,pk}$ (which we only estimate via the approach of section 4) and on the input electric field profile (which is not known for these experiments). For Fig. 6(b) we added a small, smooth and monotonic frequency-dependent offset to the effective index in order to shift the cascaded DFG peak to $2.85 \mu\text{m}$. We chose a functional form $\delta n(\omega) = \frac{1}{2}[1 + \tanh((\omega_L - \omega)/\Delta\omega)][(\omega - \omega_L)/(\omega_{OH} - \omega_L)]^2 \delta n_0$, where ω_L and ω_{OH} corresponding to $2 \mu\text{m}$ and $2.85 \mu\text{m}$, respectively, $\Delta\omega = 2\pi \times 5 \text{ THz}$, and $\delta n_0 = -8 \times 10^{-4}$. This functional form was chosen so that $\delta n \approx \delta n_0$ at $2.85 \mu\text{m}$, and so that $\delta n \approx 0$ for wavelengths $< 2 \mu\text{m}$, where our waveguide dispersion model is well-calibrated. This latter constraint helps to ensure that the pulse dynamics are not artificially altered by the effective index offset. Provided the above constraints are met, we have found that the spectrum is relatively insensitive to the functional form of $\delta n(\omega)$. With improved characterization of the RPE waveguide dispersion and the nonlinear parameters of the model, and the input pulse, this offset might not be required.

In comparing this work with prior modeling of the experiments of Ref. [1], we note that Refs. [8, 13] also show good agreement between single-envelope simulations and the 1580-nm-pumped experiments we have discussed in this section, despite their neglect of the waveguide mode profiles and Raman nonlinearities. Without both the χ_E and $\chi_{R,pk}$ terms, only the cascaded- $\chi^{(2)}$ interactions contribute to the total SPM, and so $\chi_{\text{total}}^{(3)}$ is much larger. For a plane-wave model, $c_q = 1$ for $q = 0$ and is zero otherwise (see appendix B), and hence $\chi_{\text{cascade}}^{1,0} = -5170 \text{ pm}^2/V^2$, from Table 3 and Eq. (16). We found earlier in this section that $\chi_{\text{total}}^{(3)} \approx -626 \text{ pm}^2/V^2$. Therefore, neglecting $\chi^{(3)}$ and waveguide modes yields an effective low-frequency $\chi^{(3)}$ that is an order of magnitude too large for these particular experiments. If $\chi^{(3)}$ and waveguide effects are neglected, the SPM is increased by a similar factor, which will substantially alter the dynamics. For some cases, the measured spectrum can still be recovered by treating the pulse intensity as an unconstrained fit parameter in the simulations, but such an approach would not work in other spectral ranges, such as those considered in section 3.

In contrast to the plane-wave models of previous work, for Fig. 6(b) we included appropriate modal overlaps and $\chi^{(3)}$ terms according to Eq. (5), and we assumed a pulse energy of 1.2 nJ at the input to the waveguide, the same as the experimental value. In section 4, we also showed that properly-calibrated third-order nonlinear effects, particularly SRS, are required to model the 1043-nm-pumped experiments of [1]; these experiments were not modeled in Refs. [8, 13].

6. Discussion

We have shown that our nonlinear waveguide model, given in Eq. (5), is in good agreement with the experimental results of Ref. [1] with both 1580 nm and 1043 nm pumps, and both uni-

form and chirped QPM gratings. The $\chi^{(2)}$, instantaneous $\chi^{(3)}$, and stimulated Raman scattering nonlinearities are all essential for accurately modeling the supercontinuum generation process.

To improve the accuracy of the simulations, the size of the various nonlinear terms (the susceptibilities themselves, and subsequent modal overlap integrals) in RPE waveguides must be known more precisely, especially the third-order nonlinear susceptibilities. Determining χ_E and $\chi_{R,pk}$ more accurately via direct measurements will be the subject of future work. The dispersion of the nonlinear susceptibilities is important as well, as shown in section 5. It may also be important to determine the dispersion of the RPE waveguides at long wavelengths with greater accuracy. In addition to the model parameters in Eq. (5), measurements of the complex input electric field are needed; plausible values of the pulse chirp, which we assumed to be zero in our simulations, can have a significant impact on the output spectrum. Measurement of the spatial mode content of the output electric field would also be useful since this would help to indicate which waveguide modes are important and must be included in the model.

Despite the difficulties in fully calibrating the parameters entering into Eqs. (5), our model is sufficiently accurate to be used to analyze and design QPM gratings and waveguides in order to improve spectral broadening or to perform other ultrafast functionalities such as nonlinear pulse compression. For example, we have shown that for both of the experiments of Ref. [1], the cascaded- $\chi^{(2)}$ and $\chi^{(3)}$ susceptibilities were of comparable magnitude but opposite sign, and hence competed with each other. This cancellation of contributions to $\chi_{\text{total}}^{(3)}$ significantly reduces the rate of SPM and hence increases the energy requirements for supercontinuum generation. Furthermore, based on our simulations, in the 1043-nm-pumped case the reduced rate of SPM meant that a strong FH pulse had to be used, which in turn led to a strong generated SH pulse; this SH pulse amplified quantum noise, which led to incoherent supercontinuum generation.

In fiber-based supercontinuum generation, the zero group velocity dispersion (GVD) wavelength, λ_{GVD} , is often shifted by waveguide design to be nearby the input wavelength, λ . We have seen from simulations based on Eqs. (5) that shifting λ_{GVD} to be comparable to the input wavelength is one way to significantly enhance the spectral broadening processes for $\chi^{(2)}$ -based continua as well, since generated spectral components would then remain overlapped temporally. Furthermore, if the GVD at the input wavelength is negative ($\lambda > \lambda_{\text{GVD}}$) or negligible ($\lambda \approx \lambda_{\text{GVD}}$), supercontinuum generation could be achieved with a positive $\chi_{\text{total}}^{(3)}$; for this case, by choosing $\Delta k_{1,000} < 0$ the contributions of $\chi^{(2)}$ and $\chi^{(3)}$ to SPM would add rather than cancel while still being of appropriate sign to support $\chi^{(3)}$ -like bright solitons at the input wavelength.

Since RPE waveguides are weakly guiding, significant shifts in λ_{GVD} cannot be obtained. However, λ_{GVD} is conveniently located near 2 μm , making Tm-based laser sources promising candidates for increased spectral broadening in RPE waveguides [28]. An alternative approach is to use tightly confining waveguides, in which a high index contrast could enable shifting λ_{GVD} to the 1.55- μm and 1- μm spectral regions. There is also the possibility of using AlGaAs QPM waveguides, which can be tightly confining and are transparent in the mid-IR. With simultaneous engineering of the waveguide dispersion and the QPM grating, supercontinuum generation may be possible across the mid-IR. With the model of nonlinear interactions in QPM waveguides we have developed here, strategies can be developed for reaching spectral regions not accessible to silica-fiber-based supercontinuum sources, and for performing optimizations made possible by the versatility of QPM gratings [14, 23], suggesting a path towards compact and robust traveling-wave frequency comb sources in the IR and mid-IR spectral regions.

A. Material properties

In this appendix, we discuss the nonlinear coefficients contained in Eqs. (5); these must be known accurately in order to quantitatively predict experimental results. For the second-order nonlinear terms in this appendix, we assume $d_{33} = 25.2$ pm/V for 1064-nm-SHG [26]; for

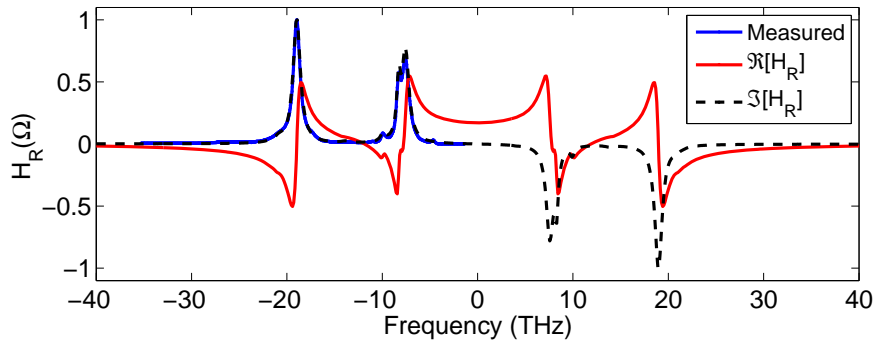


Fig. 7. Measured imaginary and complex reconstructed stimulated Raman scattering transfer function for e-wave interactions in LiNbO₃, based on our XZZ \bar{X} spontaneous Raman scattering measurement. The quality of the fit implies that a sum of Lorentzians is a suitable model for $\Im[H_R]$, so we calculate $\Re[H_R]$ from these fit parameters (dashed red line).

modeling the experiments of Ref. [1], we assume $d_{33} = 25.2$ pm/V for 1043-nm-pumping and $d_{33} = 19.5$ pm/V for 1580-nm-pumping [26]. We also assume that $\chi^{(2)}(x, y) = 0$ close to the upper surface of the crystal, as described in section 2.

We determined the imaginary part of the normalized Raman transfer function, $\Im[H_R]$, by measuring the spontaneous Raman scattering cross section of congruent LiNbO₃ (CLN). The Raman spectrum of LiNbO₃ has been measured previously [29, 30], but in some cases large relative errors have been reported [29]; an additional measurement across the Raman spectrum could prove to be useful. For the measurement, we used a WiTec Alpha300 S Raman microscope in the XZZ \bar{X} configuration and at 295 K. The resulting spectrum is shown in Fig. 7 (blue line). To determine $\Re[H_R]$ we fitted the measured $\Im[H_R]$ to a sum of Lorentzians; this reconstructed Raman susceptibility is also shown in Fig. 7. The parameters for the fit are given in Table 1. The terms of the Lorentzian fit have form $a_j/(f_j^2 - f^2 + 2i\gamma_j f)$ for optical frequency f (not angular frequency). The small measured peak at around -4.6 THz (≈ -153 cm⁻¹) was neglected in the fit since it does not correspond to the e-wave polarization component [31]: its presence indicates imperfect polarization discrimination during the measurement.

Table 1. Lorentzian Fit Parameters for $H_R(\Omega)$

f_j (THz)	7.59	8.28	9.93	18.98	20.93	21.52	20.62
γ_j (THz)	0.453	0.222	0.255	0.461	0.278	0.485	0.282
a_j (a.u.)	0.268	0.085	0.019	1.000	0.013	0.014	0.012

Calibrating the $\chi^{(3)}$ coefficients in LiNbO₃ can be challenging, as noted in Ref. [32]. In the remainder of this appendix, we discuss the absolute scale of the third-order nonlinear coefficients $\chi_{R,pk}$ and χ_E . The nonlinear refractive index, n_2 , is related to the third-order nonlinear susceptibility. However, there are at least three significant contributions to n_2 : the instantaneous χ_E susceptibility, the real part of the χ_R susceptibility, and also an effective $\chi^{(3)}$ susceptibility, denoted $\chi_{\text{eff}}^{(3)}$, which arises due to the phase mismatched second-order nonlinear interaction, i.e. the cascaded $\chi^{(2)}$ process [32,33]. In order to determine χ_E from n_2 , each of these contributions must be accounted for.

In Ref. [25], n_2 was measured for LiNbO₃ with the Z-scan method using 30-ps (FWHM) pulses with a center wavelength of 1.064 μm . Since the reconstructed LiNbO₃ Raman spectrum

in Fig. 7 does not vary significantly for frequencies < 1 THz, and assuming the 30-ps pulses had bandwidths ≤ 1 THz, the measured n_2 represented the total low-frequency-shift $\chi^{(3)}$ response, given by $\chi_0^{(3)} = \chi_E + \chi_{R,pk} H_R(0) + \chi_{\text{cascade}}^{(3)}$. This total response can be calculated from n_2 as

$$\chi_0^{(3)} = \frac{4}{3} n_2 n_{FH}^2 \epsilon_0 c, \quad (8)$$

which in LiNbO₃ is given by $\chi_0^{(3)} \approx 1575 \text{ pm}^2/\text{V}^2$ for $n_2 = 0.933 \times 10^{-6} \text{ cm}^2/\text{GW}$ [25]. The contribution to $\chi_0^{(3)}$ from the cascaded $\chi^{(2)}$ interaction is given, via multiple scale analysis [34], by

$$\chi_{\text{cascade}}^{(3)} = -\frac{16\pi d_{\text{eff}}^2}{3n_{SH}\lambda_{FH}} \frac{1}{\Delta k}. \quad (9)$$

For the Z-scan configuration used for LiNbO₃ in Ref. [25], $d_{\text{eff}} = d_{33}$ and $\Delta k = k(2\omega) - 2k(\omega) = 0.927 \mu\text{m}^{-1}$ for 1.064- μm pumping [35], and so $\chi_{\text{cascade}}^{(3)} \approx -4830 \text{ pm}^2/\text{V}^2$. Importantly, $\chi_{\text{cascade}}^{(3)}$ is of opposite sign to the electronic and Raman contributions. After subtracting the contribution of the cascading term (which can be characterized more easily since d_{33} is relatively well-known), we find that $\chi_E + \chi_{R,pk} H_R(0) = 6365 \text{ pm}^2/\text{V}^2$, much larger than $\chi_0^{(3)}$.

Additional measurements are needed to determine both χ_E and $\chi_{R,pk}$. One way to determine $\chi_{R,pk}$ separately from χ_E is by measuring the SRS gain at Ω_{pk} . However, tabulated values for the Raman gain coefficient are inconsistent with the n_2 measurements described above. Consider the Raman gain coefficient, (g_S/I_L) , evaluated at Stokes frequency $\omega_S = \omega_L - \Omega_{pk}$ for some pump laser frequency ω_L . It can be shown from Eq. (5) that

$$\chi_{R,pk} = \frac{n_S n_L \epsilon_0 c \lambda_S}{3\pi} \frac{g_S}{I_L}, \quad (10)$$

where the reduction in gain due to Stokes-anti-Stokes coupling effects are neglected when defining (g_S/I_L) , and n_S and n_L are the refractive indices at the Stokes and pump wavelengths, respectively. In LiNbO₃ with a 1.064- μm pump laser, the gain coefficient corresponding to a contribution of 100% from SRS to the value of $\chi_0^{(3)} - \chi_{\text{cascade}}^{(3)} = 6365 \text{ pm}^2/\text{V}^2$ calculated above is given by $(g_S/I_L)_{\text{max}} \approx 2.51 \text{ cm/GW}$, using $H_R(0) = 0.17$ from Fig. 7. However, the gain coefficient tabulated in Ref. [36] is 9.4 cm/GW at 694 nm [36], which corresponds to 6.1 cm/GW at 1.064 μm (by scaling with optical frequency); this value is more than twice as large as the upper bound for (g_S/I_L) provided by the n_2 measurement (assuming $\chi_E > 0$).

The tabulated values for (g_S/I_L) are also inconsistent with recent experiments with intense IR pulses. The Raman gain rate g_R , in cm^{-1} , can be approximated as [36]

$$g_R \approx 2\Re \left[\sqrt{-ig_S \Delta k_R / 2 - (\Delta k_R / 2)^2} \right], \quad (11)$$

where g_S is the coupling coefficient between the intensity at the Stokes shifted wave at ω_S and the pump laser at $\omega_L = \omega_S + \omega_{R,pk}$, and the phase mismatch $\Delta k_R \equiv 2k(\omega_L) - k(\omega_S) - k(\omega_{AS})$ for anti-Stokes frequency ω_{AS} . In turn, g_S is determined via the Raman gain coefficient (g_S/I_L) . In Refs. [24, 37], a 1-cm-long MgO:LiNbO₃ crystal was pumped with 1.064- μm pulses with intensities of $> 7 \text{ GW/cm}^2$ and durations of 12 ps (FWHM); the corresponding pulse bandwidth was significantly narrower than the linewidth of the main peaks of $H_R(\Omega)$ shown in Fig. 7. Assuming $(g_S/I_L) = 6.1 \text{ cm/GW}$, Eq. (11) predicts an SRS gain in this case of 136 dB (185 dB if $\Delta k_R \rightarrow \infty$). Despite this high predicted gain, no Stokes wave was observed experimentally. If

we instead assume the n_2 -based upper bound on (g_S/I_L) of 2.51 cm/GW, the gain at the Stokes frequency would be approximately 69 dB.

Based on the above considerations, it is difficult to use available literature data to absolutely calibrate the third-order nonlinear coefficients in LiNbO₃ (which could also be different from those of RPE LiNbO₃). The peak Raman susceptibility $\chi_{R,pk}$ can be bounded above by the nonlinear refractive index and by the absence of SRS in the high intensity experiments discussed, and $\chi_{R,pk}H_R(0) + \chi_E$ can be estimated from the measured value of n_2 . For this paper, we further constrain the susceptibilities to yield output spectra in quantitative agreement with the super-continuum generation experiments of Ref. [1], which we model in Sections 5 and 3. The $\chi^{(3)}$ values that we use are given by $\chi_{R,pk} = 5.3 \times 10^3 \text{ pm}^2/\text{V}^2$, and $\chi_E(1043 \text{ nm}) = 5.46 \times 10^3 \text{ pm}^2/\text{V}^2$; these parameters are discussed further in section 4. For the 1580-nm-pumping case discussed in section 5, χ_E is scaled according to theoretical predictions [25], such that $\chi_E(1580 \text{ nm})/\chi_E(1043 \text{ nm}) \approx 0.8$.

Lastly, note that in Ref. [25] there was a significant discrepancy between measurements of n_2 and a theoretical calculation based on a simplified two-band model: at 532 nm, the measured n_2 was approximately $9.1 \times$ the value at 1064 nm, while the two-band theory predicted a scaling factor of only 2.5. A possible resolution to this discrepancy is that there is a large negative contribution to n_2 from $\chi_{\text{cascade}}^{(3)}$ in the 1064-nm case but not in the 532-nm case. Since 532 nm lies above half the LiNbO₃ bandgap, it has a very large phase mismatch with its second harmonic at 266 nm [38], so the contribution to n_2 from $\chi_{\text{cascade}}^{(3)}$ is much smaller. Given the scaling of χ_E with frequency, the additional 532-nm data point for n_2 is sufficient, in principle, to determine both χ_E and $\chi_{R,pk}$ at 1.064 μm . With the measured value of $n_2 = 8.25 \times 10^{-6} \text{ cm}^2/\text{GW}$, $\chi_0^{(3)}(532 \text{ nm}) = 14.6 \times 10^3 \text{ pm}^2/\text{V}^2$. If we assume that $\chi_{\text{cascade}}^{(3)}(532 \text{ nm}) = 0$ and that $\chi_{R,pk} = 5.3 \times 10^3 \text{ pm}^2/\text{V}^2$ is non-dispersive, then $\chi_E(532 \text{ nm}) = 13.4 \times 10^3 \text{ pm}^2/\text{V}^2$, and $\chi_E(532 \text{ nm})/\chi_E(1064 \text{ nm}) \approx 2.5$, in good agreement with the (oversimplified) two-band model.

B. Cascading approximation for QPM waveguides

In the limit of a large phase mismatch, $\chi^{(2)}$ interactions can be approximated by $\chi^{(3)}$ -like self- and cross-phase-modulation (SPM and XPM) terms; this approach is termed the cascading approximation, and has been discussed extensively [33]. In Appendix A, we used this approximation to constrain the $\chi^{(3)}$ susceptibilities given a known nonlinear refractive index. In this appendix, we determine the cascading approximation for the case of QPM waveguide interactions. This calculation gives a total effective $\chi^{(3)}$, denoted $\chi_{\text{total}}^{(3)}$, which determines the rate of SPM for narrow-bandwidth pulses. In the experiments modeled in sections 3 and 5 the conditions for the validity of the approximation are not always satisfied for all of the waveguide modes and QPM orders, but it nonetheless provides valuable insight into the pulse propagation dynamics (especially near the start of the QPM grating),

In Ref. [34], the cascading approximation was determined from coupled wave equations for SHG via a multiple-scale analysis. A similar procedure can be used to determine the cascading approximation for QPM waveguides based on Eq. (5). To proceed with the analysis, we first split each mode envelope A_n into first harmonic (FH) and second harmonic (SH) pulse components $A_n^{(FH)}$ and $A_n^{(SH)}$, with carrier frequencies ω_{FH} and $\omega_{SH} = 2\omega_{FH}$, respectively. In principle, Eq. (5) can give rise to pulses around carrier frequencies $m\omega_{FH}$ for all positive integers m . However, for pulses with a bandwidth $\Delta\Omega$ less than an octave, i.e. for $\Delta\Omega \ll \omega_{FH}$, often only the components around ω_{FH} and ω_{SH} are relevant, to lowest order in the perturbation. Furthermore, higher order modes around ω_{FH} can often be neglected, for example in the case when the waveguide only supports a single mode at that frequency. With these assumptions,

Eq. (5) yields the following simplified time-domain coupled wave equations for SHG,

$$\begin{aligned}
\frac{\partial A_{0,FH}}{\partial z} + \hat{D}_{0,FH} A_{0,FH} &= -i \left(\frac{\omega^2 u}{g_0 \beta_0 c^2} \right)_{\omega_{FH}} \times \\
&\left[\sum_{q,m} d_m \theta_{q00} \exp^{-i \int \Delta k_{m,q00}(z') dz'} A_{0,FH}^* A_{q,SH} + \frac{3(\chi_E + H_R(0)\chi_{R,pk})}{8} \theta_{0000} |A_{0,FH}|^2 A_{0,FH} \right] \\
\frac{\partial A_{q,SH}}{\partial z} + \hat{D}_{q,SH} A_{q,SH} &= -i \left(\frac{\omega^2 u}{g_q \beta_q c^2} \right)_{\omega_{SH}} \times \\
&\left[\sum_m d_m \theta_{q00} \exp^{i \int \Delta k_{m,q00}(z') dz'} \frac{A_{0,FH}^2}{2} + \frac{6(\chi_E + H_R(0)\chi_{R,pk})}{8} \theta_{qq00} |A_{0,FH}|^2 A_{q,SH} \right]
\end{aligned} \quad (12)$$

where the FH and SH envelopes are given in terms of the following approximate form for the spectrum of the total electric field

$$\begin{aligned}
\tilde{E}(x, y, z, \omega) &\approx \frac{1}{2} \tilde{B}_0(x, y, \omega_{FH}) A_{0,FH}(z, \omega - \omega_{FH}) \exp^{-i(\beta_0(\omega_{FH}) - \omega_{FH}/v_{ref})} + \\
&\frac{1}{2} \sum_q \tilde{B}_q(x, y, \omega_{SH}) A_{q,SH}(z, \omega - \omega_{SH}) \exp^{-i(\beta_q(\omega_{SH}) - \omega_{SH}/v_{ref})}
\end{aligned} \quad (13)$$

and $\theta_{q00} = \Theta_{q00}(\omega_{SH}, \omega_{FH})$ and $\theta_{qq00} = \Theta_{qq00}(\omega_{SH}, \omega_{SH}, \omega_{FH})$. In Eqs. (12) and (13), the spatial mode profiles and coupling coefficients have been evaluated at the optical carrier frequencies. We have also assumed that the intensity of the SH pulse is much lower than that of the FH pulse, and have therefore neglected the $\chi^{(3)}$ terms involving $|A_{n,SH}|^2$. For the purposes of this simplified analysis, we have assumed that the pulse bandwidth is narrow enough that $H_R(\Omega)$ can be approximated as $H_R(0)$; this approximation does not apply for supercontinuum generation [in the simulations, we use $H_R(\Omega)$], but is useful for estimating the rate of SPM for the FH pulse at the start of the QPM grating. The phase mismatch terms are given by

$$\Delta k_{m,q00}(z) = \beta_q(2\omega_{FH}) - 2\beta_0(\omega_{FH}) - mK_g(z) \quad (14)$$

for QPM order m and waveguide mode q of the SH pulse. If the characteristic length defined by $L_{m_1, m_2} \equiv |\Delta k_{m_1, q00} - \Delta k_{m_2, q00}|^{-1}$ is much shorter than any other characteristic lengths of the problem for all $m_1 \neq m_2$, the multiple-scale analysis can be applied. In Ref. [34], where the linear operators represented diffracting beams, the Rayleigh range would be a relevant characteristic length. For pulses, the group velocity mismatch length between the FH and SH pulses is one of several important characteristic length scales. Given a sufficiently small value of L_{m_1, m_2} for all $m_1 \neq m_2$, and assuming that there is no SH pulse input at the start of the interaction, multiple scale analysis of Eq. (12) yields

$$\begin{aligned}
\frac{A_{0,FH}}{\partial z} + \hat{D}_{0,FH} A_{0,FH} &= i \frac{\omega_{FH}}{g_{0,FH} n_{0,FHC}} \left(\sum_{m,q} \frac{d_m^2 \theta_{q00}^2 \omega_{FH}}{g_{q,SH} n_{q,SHC}} \frac{1}{\Delta k_{m,q00}(z)} \right) |A_{0,FH}|^2 A_{0,FH} - \\
&- i \frac{\omega_{FH}}{g_{0,FH} n_{0,FHC}} \left(\frac{3\theta_{0000}(\chi_E + H_R(0)\chi_{R,pk})}{8} \right) |A_{0,FH}|^2 A_{0,FH},
\end{aligned} \quad (15)$$

where $n_{q,j} = \beta_q(\omega_j)c/\omega_j$ and $g_{n,j} = g_n(\omega_j)$ for wave j ($j = FH$ or $j = SH$) and mode normalization coefficient $g_n(\omega)$ given by Eq. (4). To analyze the different terms, it is convenient

to introduce a simpler normalization of the mode profiles than the one used in sections 3 and 5 to analyze broadband pulses. If we choose $g_n(\omega) = a_n(\omega)$ instead of $g_n(\omega) = a_n(\omega)^{1/3}$, the mode profiles $B_n(x, y, \omega)$ are dimensionless. With this definition of g_n , $\theta_{0000}/g_0(\omega_{FH}) = 1$, and the total effective $\chi^{(3)}$ is given by

$$\begin{aligned}\chi_{\text{total}}^{(3)}(z) &= \chi_E + \chi_{R,pk} H_R(0) - \sum_{m,q} c_q \frac{16\pi d_m^2}{3n_{q,SH} \lambda_{FH}} \frac{1}{\Delta k_{m,q00}(z)} \\ &\equiv \chi_E + \chi_{R,pk} H_R(0) + \sum_{m,q} \chi_{\text{cascade}}^{(m,q)}(z)\end{aligned}\quad (16)$$

where the cascading reduction factors c_q are given by

$$c_q = \frac{(\int \bar{\chi} B_{FH}^2 B_{q,SH} dx dy)^2}{(\int |B_{FH}^4| dx dy) (\int |B_{q,SH}|^2 dx dy)}, \quad (17)$$

independent of the choice of normalization of the spatial mode profiles B_j ; $\bar{\chi}(x, y)$ is the transverse spatial profile of the second order nonlinear susceptibility, which appears in Eq. (3). The $\chi^{(2)}$ contributions to $\chi_{\text{total}}^{(3)}$ have forms analogous to Eq. (9). In sections 3 and 5 the values for these terms are discussed, and we show that almost complete cancellation of $\chi_{\text{total}}^{(3)}$ can occur. The parameters c_q and $\Delta k_{0,q00}$ are given in Tables 2 and 3 for the 1043-nm and 1580-nm pumped calculations discussed in sections 4 and 5, respectively.

Table 2. Cascading Approximation Parameters at 1043 nm

Mode number	0	1	2	3	4	5	6	7
$2\pi/\Delta k_{0,q00}$ (μm)	5.671	5.765	5.870	5.985	6.064	6.108	6.164	6.240
c_q	0.912	0.000	0.003	0.000	0.031	0.000	0.000	0.000

Table 3. Cascading Approximation Parameters at 1580 nm

Mode number q	0	1	2	3	4	5	9
$2\pi/\Delta k_{0,q00}$ (μm)	16.871	17.665	18.624	19.723	19.879	20.924	22.531
c_q	0.854	0.000	0.002	0.000	0.056	0.000	0.003

For bulk interactions, $\chi_{\text{cascade}}^{(3)}$ can be found by taking $c_q = \delta_{q0}$ and $d_m = \delta_{m0} d_{33}$ where δ_{ij} is the Kronecker delta. To calculate the cascaded phase shifts, we assumed a pulse centered around a particular carrier frequency. However, some care should be taken with this procedure since during the supercontinuum generation process the center frequency of the pulse can shift. This frequency shift can reduce the accuracy of the cascading approximation for terms that are nearly phasematched. For the simulations performed here, we add $\sum \chi_{\text{cascade}}^{m,q}$ to the instantaneous third-order nonlinear coefficient χ_E , with summation performed over all terms except those which are either explicitly included in Eq. (5) or for which $m = 1$.

Acknowledgments

This research was supported by the U.S. Air Force Office of Scientific Research (AFOSR) under grants FA9550-09-1-0233 and FA9550-05-1-0180.